

# Optics Letters

## Depth-resolved optimization of a real-time sensorless adaptive optics optical coherence tomography

ACNER CAMINO,<sup>1</sup> RINGO NG,<sup>2</sup> JOEY HUANG,<sup>2</sup> YUKUN GUO,<sup>1</sup> SHUIBIN NI,<sup>1</sup> YALI JIA,<sup>1,3</sup> DAVID HUANG,<sup>1</sup> AND YIFAN JIAN<sup>1,3,\*</sup>

<sup>1</sup>Casey Eye Institute, Oregon Health and Science University, Portland, Oregon 97239, USA

<sup>2</sup>School of Engineering Science, Simon Fraser University, Burnaby, Canada

<sup>3</sup>Department of Biomedical Engineering, Oregon Health and Science University, Portland, Oregon 97239, USA

\*Corresponding author: jian@ohsu.edu

Received 11 February 2020; revised 3 April 2020; accepted 7 April 2020; posted 9 April 2020 (Doc. ID 390134); published 30 April 2020

**Sensorless adaptive optics optical coherence tomography (AO-OCT) is a technology to image retinal tissue with high resolution by compensating ocular aberrations without wavefront sensors. In this Letter, a fast and robust hill-climbing algorithm is developed to optimize five Zernike modes in AO-OCT with a numerical aperture between that of conventional AO and commercial OCT systems. The merit function is generated in real time using graphics processing unit while axially tracking the retinal layer of interest. A new method is proposed to estimate the largest achievable field of view for which aberrations are corrected uniformly in sensorless AO-OCT.** © 2020 Optical Society of America

<https://doi.org/10.1364/OL.390134>

Adaptive optics optical coherence tomography (AO-OCT) is a technology to achieve high lateral resolution imaging of the retinal tissue by compensating ocular aberrations [1]. Despite the outstanding resolution achieved with AO-OCT, its translation from bench to clinic has been challenged by a number of factors, including large instrument footprint, high cost, narrow field of view (FOV), and limited depth of focus. In addition, AO-OCT has historically required long imaging sessions and very cooperative subjects. The purpose of this Letter is to improve the sensorless AO-OCT aberration estimation aiming to overcome some of the challenges of AO-OCT clinical translation. We will demonstrate an aberration correction method based on adaptive hill-climbing optimization of merit functions (MFs) generated in real time on graphics processing unit (GPU) and calculated by projections of OCT reflectance at a rate of 33 volumes per second while axially tracking the retinal depth of interest.

Wavefront sensors used to measure the optical aberrations of the eye increase the cost and footprint of the instrument and reduce the optical efficiency of the sample arm; their accuracy is vulnerable to specular reflections from the lenses commonly used in an OCT sample arm. Conversely, sensorless AO-OCT can estimate aberrations by producing volumetric OCT images in real time and generating MFs based on image brightness to

guide optimization algorithms. This process is typically slower than sensor-based optimizations. Because the main disadvantage of sensorless AO-OCT is its relatively slow convergence, a fast and robust aberration estimation algorithm is paramount in sensorless schemes. An exhaustive search of the maximum value of the MF across the entire dynamic range of deformable mirror peak-to-valley strokes for each Zernike mode (i.e., coordinate search [2]) is slow and not feasible for clinical applications. The optimization algorithm we propose here used a hill-climbing approach with an adaptive step size [3] based on the cumulative gradient sign, which searched for the optimal MF of five Zernike modes sequentially (Fig. 1).

Hill climbing was assisted by parabolic fitting of the objective function and converged within a maximum of nine steps before proceeding to optimize the next mode. This scheme avoided hysteresis effects caused by large peak-to-valley stroke returns from the maximum permitted. Moreover, incremental hill-climbing steps ensured the search was restricted to the dynamic range of the deformable mirror and guaranteed enough signal-to-noise ratio to segment the depth of interest accurately, thereby producing reliable MFs of arbitrary depths to guide the optimization. A total of five modes were optimized in 1.35 s, considerably less than the time of average tear film breakup [4].

The algorithm was implemented in a spectral-domain sensorless AO-OCT prototype with a deformable mirror used as wavefront-correction element (DM69, ALPAO), for which a Zernike-to-command matrix was calibrated by the factory. The illumination beam of most ophthalmic OCT devices is typically 1.0–1.3 mm in diameter, for which ocular aberrations other than defocus have a negligible effect [5]. Larger diameters allow higher lateral resolution using AO, but reduce the achievable FOV, typically limited between 0.5–2° for a pupil size of 6 mm [6,7]. Here we chose a 3.2 mm beam at pupil [8] as a tradeoff on lateral resolution to increase the FOV of AO-OCT for the imaging of inner retinal elements (e.g., capillaries, nerve fibers) and the photoreceptor mosaic outside the central macula. The instrument's central wavelength was 840 nm with a 91 nm bandwidth. The power incident on cornea was 0.77 mW.

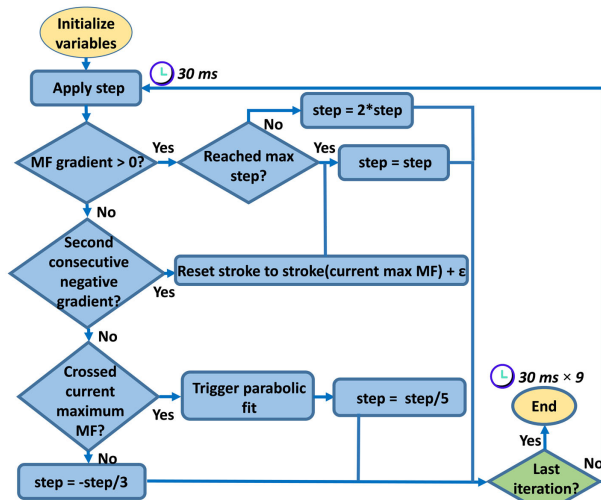


**Fig. 1.** Hill-climbing algorithm optimization of one Zernike mode. Every 30 ms a MF value is generated by the average projection of a depth-resolved slab of interest from real-time OCT volumes computed in GPU. An adaptive step is applied to the deformable mirror stroke depending on the sign of the MF gradient. Nine MFs are sampled per Zernike mode. A parabolic fit triggered by a simultaneous negative gradient and crossing of the current maximum MF estimates an optimal stroke that is never outside the mirror's dynamic range. A special case is included at the event of two consecutive negative gradients to exit noise plateaus. The number of iterations, maximum step allowed, and value of  $\epsilon$  were obtained empirically from a model eye. The process was repeated for five Zernike modes.

The lateral resolution was 6  $\mu\text{m}$ , and the estimated depth of focus was 58  $\mu\text{m}$ .

The deformable mirror had 69 elements and could adjust up to 36 Zernike modes. Given the intermediate numerical aperture, only five modes were optimized—i.e., defocusing, oblique astigmatism, vertical astigmatism, horizontal coma, and vertical coma—in order to complete the optimization in a reasonable time. With an A-line acquisition speed of 250 kHz, 33 volumes could be acquired in the wavefront optimization process (high-speed mode) prior to acquisition, using a bidirectional scanning pattern and a scanning density of 150 A-lines per B-scan and 50 B-scans per volume. The deformable mirror allows defocus/astigmatism peak-to-valley strokes larger than 25  $\mu\text{m}$ , with a resonant frequency of 1.2 kHz and a maximum settling time of 450  $\mu\text{s}$ . The volumes acquired in a high-speed mode had higher sampling density in the fast-scanning direction than the low scanning direction to ensure accurate tracking of the layer of interest in real time on a B-scan basis. The mean value of the reflectance projection within the slab of interest was used as a MF. OCT volumes were processed in real time with our GPU OCT software on a batch basis [9], and the batch processing scheme allowed a relatively short overhead between acquisition and processing which is crucial for image-based sensorless AO.

The optimization of the adaptive hill-climbing algorithm converged close to the peak of the objective function characterized by an exhaustive coordinate search within nine sampling points (Fig. 2). The sequential optimization of five modes for the ellipsoid (EZ) zone and the outer plexiform layer (OPL) are shown in Fig. 3. Boundaries on the search of Zernike mode

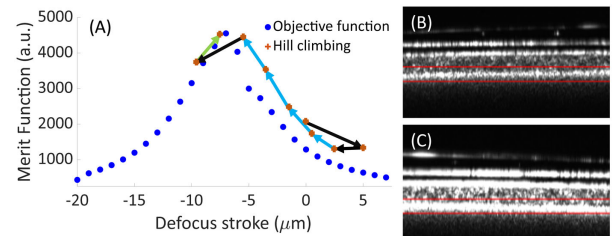


**Fig. 2.** Performance of hill-climbing optimization. (A) Coordinate search (dark blue dots) characterizing the objective function of defocus in a model eye by iterating through the entire dynamic range of the deformable mirror. Hill-climbing starting from zero stroke converged close to the maximum value of the MF within nine iterations. The light blue and black arrows represent positive and negative gradients of the MF, respectively. The green arrow indicates that the parabolic fit was triggered, reaching the maximum of the objective function at a peak-to-valley stroke =  $-7 \mu\text{m}$ . OCT reflectance before optimization (B) increased after hill climbing was applied (C). It should be noted that previous sensorless AO-OCT papers have called coordinate search methods by the name of hill climbing [12,13].

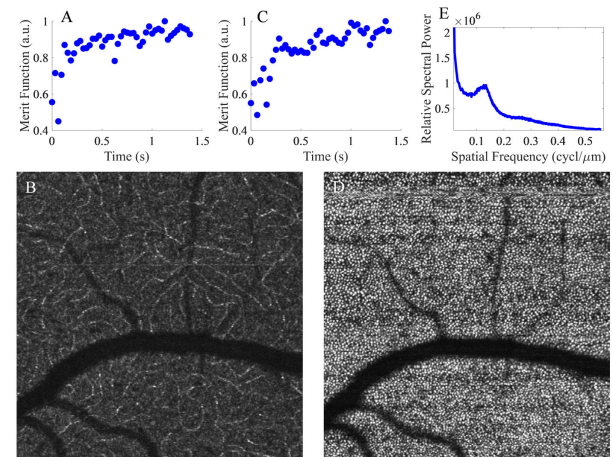


**Fig. 3.** Adaptive-step hill-climbing optimization of a MF based on the reflectance of (A), (B) depth-tracked OPL and (C), (D) EZ at an eccentricity of 5 deg superior to the fovea. (E) Yellot's ring peak corresponding to photoreceptors in (D).

amplitudes were imposed according to measured system aberrations and literature reports of the aberration ranges found in human eyes [10,11]. Subjects could blink between the aberration estimation routine and the AO-OCT acquisition. The objective function was unimodal for all modes optimized and highly reproducible between blinks (Fig. 4).

Sensorless AO [13,14] can approximate aberrations numerically, but needs real-time generation of reliable MFs to guide the optimization routine. Due to the limited depth of focus of AO-OCT, a MF guiding the wavefront phase optimization process should be computed using information restricted to the layer under scrutiny—photoreceptors, ganglion cells, nerve fibers, etc.—located at different retinal depths. The importance of optimizing the appropriate depth has been recognized since the pioneering works in AO-OCT of the past decade [15]. Axial tracking of the layer of interest was achieved here by locating the brightest layer across the B-scan and applying user-selected



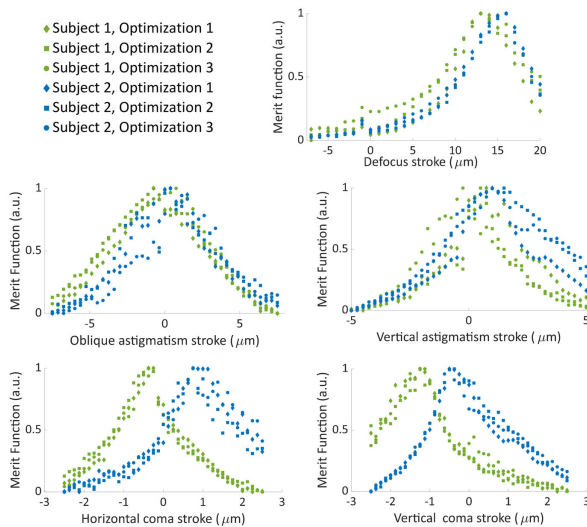


**Fig. 4.** Evaluation of the stability of the MF calculated in real time by the median of *en face* projection of the volumetric slab of interest *in vivo* in a healthy eye. For the five Zernike modes used throughout this Letter, the Zernike mode amplitude was swept stepwise across the dynamic range of the deformable mirror. This was repeated three times separated by a blink for two eyes, each time describing a unimodal objective function and converging to the same peak-to-valley stroke within a standard deviation margin of 0.5  $\mu\text{m}$ .

axial offset [16]. Higher sensitivity to eye motion, occasional errors in real-time segmentation of the retinal depth of interest, and the finite settling time of the deformable mirror limit the robustness of relying on single B-scans for wavefront optimization. The “volumetric” MF used here demonstrated excellent reproducibility [Fig. 5(A)] and allowed visualization of individual nerve fibers and photoreceptors at 5 deg eccentricity nasal from the fovea center [Figs. 5(B)–5(I)]. Because the depth of focus for the 3.2 mm beam is 58  $\mu\text{m}$ , layer-specific focusing was critical for high-resolution visualization of inner/outer retinal elements. If the retinal depth was not accounted for in the MF, the optimization was biased to the photoreceptors.

In a population of seven eyes with a refractive error between 0 and 3 diopters and astigmatism in a range of 0 to 0.5 diopters, the focusing correction step improved the MF value by (mean  $\pm$  standard deviation)  $30\% \pm 24\%$  ( $p < 0.01$ ), improved the oblique astigmatism correction by  $10 \pm 8\%$  ( $p < 0.01$ ), improved the vertical astigmatism correction by  $29\% \pm 22\%$  ( $p < 0.01$ ), improved the horizontal coma correction by  $7\% \pm 15\%$  ( $p < 0.01$ ), and improved the vertical coma correction by  $3\% \pm 6\%$  ( $p < 0.01$ ). After optimization and acquisition, image quality could be evaluated by brightness, calculated as the averaged reflectance value; contrast, calculated as the standard deviation of the reflectance value; and sharpness, calculated as the mean gradient  $G$  as  $\sum \sum \frac{\sqrt{G_x^2 + G_y^2}}{m \times n}$ , where  $m$  and  $n$  are the number of pixels over  $x$  and  $y$  axes, respectively. The brightness, contrast, and sharpness of the NFL in NFL-specific optimization were improved by  $49\% \pm 29\%$ ,  $30\% \pm 39\%$ , and  $33\% \pm 31\%$ , respectively, with respect to EZ-specific optimization, whereas for the EZ in EZ-specific optimization they were improved by  $21\% \pm 44\%$ ,  $38\% \pm 50\%$ , and  $51\% \pm 52\%$ , respectively, with respect to NFL-specific optimization.

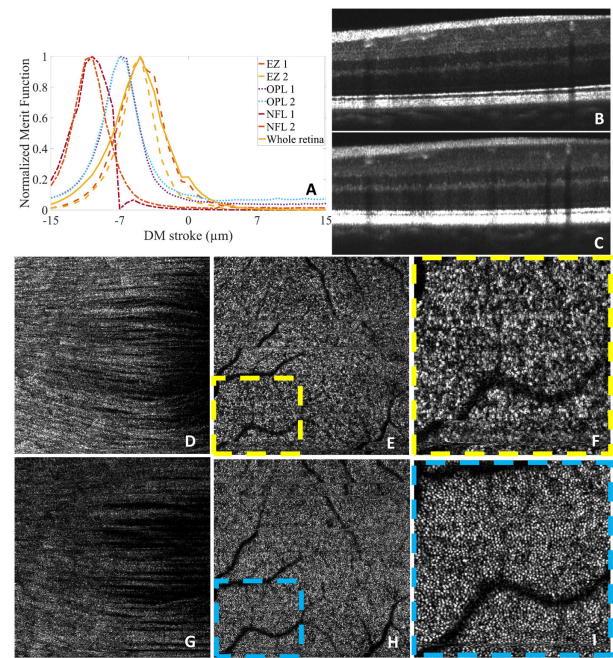


**Fig. 5.** Effect of axial tracking on optimization of ocular aberrations of a healthy eye by a sensorless AO-OCT prototype. The depth of focus in AO-OCT is not sufficient to maintain the whole retina on focus. (A) Coordinate search analysis of the deformable mirror stroke necessary to achieve focus control at three different retinal depths: nerve fiber layer (NFL), OPL, and EZ. Optimization without axial tracking (whole retina) conducted to biased optimization of the EZ, which would be detrimental for visualization of inner retinal structures. (B), (D)–(F) and (C), (G)–(I) are examples of hill-climbing optimization of the five Zernike modes in Fig. 4 for the NFL and EZ, respectively. The FOV is 4.5 deg. (F) and (I) are the yellow and blue areas in (E) and (H) covering a 2 deg FOV, zoomed in for improved visualization of the photoreceptor mosaic. (D)–(F) show optimization for NFL depth with defocused EZ, while (G)–(I) show optimization for EZ depth with defocused NFL.

A significant hurdle to the successful clinical translation of AO-OCT is its limited FOV. Although it is possible to montage adjacent scans, the number of needed acquisitions can be reduced, if each scan is acquired over the maximum FOV for which aberrations can be uniformly compensated. Such FOV can be defined as the area over which aberrations do not change significantly. Thus, we found the maximum area over which rectangular section sub-FOVs contained in the *en face* reflectance projection describe the same aberration evolution as a reference central window. This approach considerably reduces the number of volumetric scans in a high-speed mode that would otherwise be necessary to characterize each aberration for each possible FOV with coordinate search sweeps. A  $3 \times 3 \text{ mm}^2$  FOV was optimized with hill climbing, and the MF evolution over time was analyzed for sub-FOVs (Fig. 6). The MF [Fig. 6(G)] of the central  $1 \text{ mm} \times 1 \text{ mm}$  FOV was cross-correlated with external rectangular sections [Fig. 6(F), e.g., the area between blue and red, red and orange] to determine whether their trends can be considered the same (cross-correlation  $> 0.95$ ). By this method, the maximum FOV was determined for arbitrary retinal curvatures prior to acquisition.

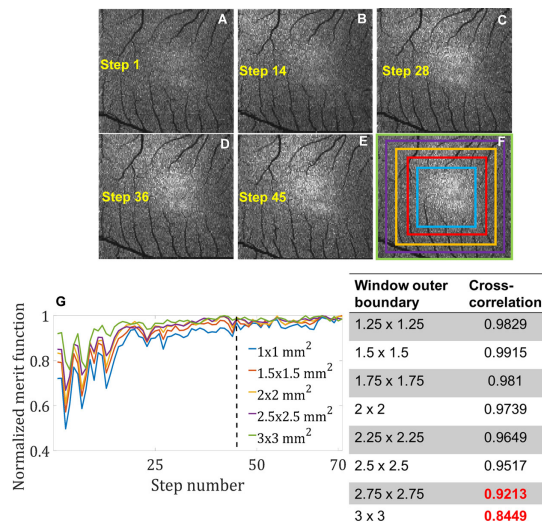


**Fig. 6.** Proposed method to determine the maximum FOV recommended in a sensorless AO-OCT instrument. (A)–(E) Evolution of *en face* reflectance projections of a 3 × 3 mm area scanned in a high-speed mode. (F) Division of sub-FOVs marked in the colored scheme represented in (G). The dashed line represents the end of the optimization routine. To assess stability, 27 additional MFs were acquired without modifying the deformable mirror configuration. MFs were computed for each digitally cropped sub-FOV in (F), excluding the pixels contained in the largest inscribed sub-FOV and normalized to each of their maximum values. The signals of the rectangular sections of arbitrary size were then cross-correlated with the signal of the central 1 mm × 1 mm. As observed in the table, the cross-correlation of the MF of the central square with the MFs of the rectangular sections between 2.5 mm × 2.5 mm and the 3 mm × 3 mm squares (red font) were lower than 0.95. A maximum FOV of about 2.5 mm × 2.5 mm would be acquired.

MFs guiding sensorless AO-OCT should be robust to noise such as fixation drifts, potential tracking errors of the layer of interest, and microsaccadic motion during the 1.35 s of optimization. In addition, and as seen in the *en face* projections generating the MF [Figs. 6(A)–6(F)], large vessel sections entering and exiting the FOV due to drifts can cause significant reflectance variations, potentially affecting the reproducibility of the MF, which is computed by averaging reflectance values. A factor that allowed good stability was calculating the MF from volumetric projections rather than individual B-scans. By tracking the MF over 27 consecutive measurements after completing optimization and without changing the deformable mirror stroke [Fig. 6(G)], we measured a coefficient of variation of only 2.5%.

A few previous optimization algorithms have been investigated to correct aberrations without wavefront sensors. Some alternatives based on gradient descent, an annealing algorithm [17], and data-based online nonlinear extremum-seeker [18] have been proposed earlier; however, they did not guarantee the convergence and were only suitable to optimize the brightest layers. Here we have shown that a MF produced with (1) reliable axial tracking of the depth of interest and (2) robust to ocular

motion during aberration correction can reliably estimate an unknown objective function *in vivo* and can be easily optimized with an adaptive-step hill-climbing approach in only 1.35 seconds. Any arbitrary retinal depth could be optimized automatically based on the corresponding depth-tracked MF, which is faster and more reliable than manual tuning by an operator in either sensor-based or sensorless AO-OCT. The ability to reliably optimize the inner retinal layers and the resolution/FOV compromise in the instrument design will make this machine and method suitable for future high-resolution imaging of inner retinal capillary flow with OCT angiography.

**Funding.** Research to Prevent Blindness (Unrestricted departmental funding grant, William Mary Greve Special Scholar Award); National Eye Institute (P30 EY010572, R01 EY023285, R01 EY024544, R01 EY027833).

**Disclosures.** Yifan Jian, Seymour Vision Inc. (I); David Huang, Optovue Inc. (F, I, P, R); Yali Jia, Optovue Inc. (F, P); Acner Camino, Optovue Inc. (P). Other authors declare no conflicts of interest.

## REFERENCES

1. M. Pircher and R. J. Zawadzki, *Biomed. Opt. Express* **8**, 2536 (2017).
2. Y. Jian, S. Lee, M. J. Ju, M. Heisler, W. Ding, R. J. Zawadzki, S. Bonora, and M. V. Sarunic, *Sci. Rep.* **6**, 27620 (2016).
3. H. Jie, Z. Rongzhen, and H. Zhiliang, *IEEE Trans. Consumer Electron.* **49**, 257 (2003).
4. M. D. P. Willcox, P. Argüeso, G. A. Georgiev, J. M. Holopainen, G. W. Laurie, T. J. Millar, E. B. Papas, J. P. Rolland, T. A. Schmidt, U. Stahl, T. Suarez, L. N. Subbaraman, O. Ö. Uçakhan, and L. Jones, *The Ocular Surface* **15**, 366 (2017).
5. L. N. Thibos, X. Hong, A. Bradley, and X. Cheng, *J. Opt. Soc. Am. A* **19**, 2329 (2002).
6. P. Bedggood, M. Daaboul, R. A. Ashman, G. G. Smith, and A. Metha, *J. Biomed. Opt.* **13**, 024008 (2008).
7. X. Jiang, J. A. Kuchenbecker, P. Touch, and R. Sabesan, *Optica* **6**, 981 (2019).
8. R. Maddipatla, J. Cervantes, Y. Otani, and B. Cense, *J. Biophotonics* **12**, e201800192 (2019).
9. Y. Jian, K. Wong, and M. Sarunic, *J. Biomed. Opt.* **18**, 026002 (2013).
10. E. J. Fernández and P. Artal, *Opt. Express* **16**, 21199 (2008).
11. A. Hartwig and D. A. Atchison, *Invest. Ophthalmol. Visual Sci.* **53**, 7862 (2012).
12. D. J. Wahl, M. J. Ju, Y. Jian, and M. V. Sarunic, *Biomed. Opt. Express* **10**, 4859 (2019).
13. M. J. Ju, M. Heisler, D. Wahl, Y. Jian, and M. V. Sarunic, *J. Biomed. Opt.* **22**, 121703 (2017).
14. M. J. Booth, *Light: Sci. Appl.* **3**, e165 (2014).
15. R. J. Zawadzki, S. M. Jones, S. S. Olivier, M. Zhao, B. A. Bower, J. A. Izatt, S. Choi, S. Laut, and J. S. Werner, *Opt. Express* **13**, 8532 (2005).
16. M. Cua, S. Lee, D. Miao, M. J. Ju, P. Mackenzie, Y. Jian, and M. Sarunic, *J. Biomed. Opt.* **21**, 026007 (2016).
17. M.-R. Nasiri-Avanaki, S. A. Hojjatoleslami, M. Paun, S. Tuohy, A. Meadway, G. Dobre, and A. G. Podoleanu, *Proceedings of Mathematical Methods and Applied Computing*, WSEAS (2009), pp. 669–674.
18. H. R. G. W. Verstraete, S. Wahls, J. Kalkman, and M. Verhaegen, *Opt. Lett.* **40**, 5722 (2015).